An improved upper boundary condition for longwave radiative flux in the stratosphere to correct model biases

Steven M. Cavallo*, Jimy Dudhia and Chris Snyder

National Center for Atmospheric Research†, Boulder, Colorado

* *Corresponding author address:* Steven Cavallo, NCAR Earth System Laboratory, 3450 Mitchell Lane, Boulder, CO 80301.
E-mail: cavallo@ucar.edu

† NCAR is sponsored by the National Science Foundation

ABSTRACT

A cold bias in potential temperature tendencies of 10 K day^{-1}, strongest at the top of the model, is observed in Weather Research and Forecasting (WRF) model forecasts. The bias originates from the longwave radiation physics scheme and can be reduced substantially by (1) modifying the treatment within the scheme of the layer between the model top and top of atmosphere, and (2) constraining stratospheric water vapor to remain within the estimated climatology in the stratosphere. These changes reduce the longwave heating rate bias at the model top to $\pm$0.5 K day^{-1}. Corresponding bias reductions are also seen, particularly near the tropopause.

1. Introduction

Use of mesoscale models has been shown to improve forecasts while providing more detailed structure of the atmosphere, particularly with regard to complex terrain (e.g., Mass et al. 2002), hurricane prediction (e.g., Davis et al. 2008), and convective systems (e.g., Weisman et al. 2008). Nevertheless, significant model biases remain. A recent application using the Weather Research and Forecasting (WRF; Skamarock et al. 2008) model and Advanced Hurricane-research WRF (AHW; Davis et al. 2008) in experiments for the 2009 Atlantic hurricane season (hereafter AHW 2009) revealed a bias in temperature, evident by a substantial cooling trend, strongest near the model top. Here, we examine this bias by re-creating AHW forecasts using the same domain (Fig. 1a) and model configuration, and initialized using Global Forecasting System (GFS) analyses.

A temperature cooling bias is evident when viewing a composite of 6-hour forecasts from

00 UTC 16 August 2009 through 00 UTC 22 August 2009. Fig. 1b shows the domain-averaged composite tendencies of potential temperature (θ) and radiative θ heating rates. The local time tendency of potential temperature ($\frac{\partial \theta}{\partial t}$) decreases from ∼0 K day^{-1} near the tropopause to -10 K day^{-1} at the top model level. Longwave heating ($\dot{\theta}_{LW}$) follows a similar pattern, but has larger magnitude in the stratosphere. At these levels, $\frac{\partial \theta}{\partial t}$ is nearly equal to the net radiative heating rate, indicating that $\dot{\theta}_{LW}$ is partially offset by shortwave heating. To verify whether $\dot{\theta}_{LW}$ exhibits a bias, standard tropical (TROP) and midlatitude summer (MLS) clear-sky longwave radiative heating profiles (Ellingson et al. 1991; Clough and Iacono 1995) are shown for comparison. WRF $\dot{\theta}_{LW}$ diverges most strongly from the standard profiles for $p < 100$ hPa, with a value of -15 K day^{-1} at 20 hPa compared to -5 K day^{-1} in the standard profiles. Therefore, the cooling trend in $\frac{\partial \theta}{\partial t}$ is a result of a bias in $\dot{\theta}_{LW}$, as high as -10 K day^{-1} and increasing towards the model top. Differences ∼250 hPa are probably due to cloud effects, which are absent in the clear-sky standard profiles.

Impacts of such a cooling trend are especially likely to be seen in applications run over long periods of time. This may include applications that use data assimilation cycling, where short-term forecasts are used as a component in estimating the model analysis. The forecasts used in AHW 2009 were initialized using an ensemble Kalman filter (EnKF) consisting of 96 members at 36-km grid spacing (Torn 2010), and analyses were cycled continuously for 4 months. Most observations were assimilated in lower atmospheric levels, leaving little opportunity for observations to correct deviations from the background in upper levels. Owing to the long cycling period of the analyses, this provides a good test case for examining longer-term impacts of the model bias.

A time–height section of the EnKF background θ bias for a 3-week period are shown in

Fig. 1c. Biases are computed with respect to GFS (EnKF − GFS) for the period shown, and the data are filtered to exclude time-scales of 1 day or less. θ decreases most near the top of the model (Fig. 1c). A slight warming trend is evident near the tropopause for $100 < p < 250$ hPa, and ∼700 hPa. Here, we investigate the source of the θ bias and devise a method to correct it.

The biases discussed above are present when using WRF with the Rapid Radiative Transfer Model (RRTM; Mlawer et al. 1997). Model tops of mesoscale models such as WRF do not generally extend to the top of the atmosphere (TOA), and therefore assumptions must be made to estimate the top of the model radiative boundary conditions. In practice, model tops in mesoscale models range from 10-100 hPa. In the WRF version of RRTM (hereafter WRF-RRTM), the upper boundary is treated similarly to global climate models (GCMs); one level is added between the model top and top of atmosphere (TOA). In the extra layer, temperature is assumed to be isothermal, and all mixing ratios are assumed to remain constant, except O_3, which is reduced by a factor of 0.6 (Iacono et al. 2000). However, model tops in GCMs tend to be closer to the TOA, for example in the NCAR Community Atmospheric Model (CAM), where it is 2.9 hPa (Collins et al. 2006). Standard clear-sky atmospheric profiles show that temperature is nearly isothermal in the lower stratosphere, however above ∼50 hPa it increases with height to the stratopause, located near 1 hPa, by an average of ∼40 K (Fig. 2a). In addition to temperature, $\dot{\theta}_{LW}$ is expected to be most sensitive to carbon dioxide (CO_2) and H_2O, while O_3, although reaching a maximum ∼5 hPa (Fig. 2b), is a relatively weak absorber in the longwave bands (e.g. Manabe and Strickler 1964). Since CO_2 is well-mixed, and since it is evident from Fig. 2c that H_2O is well mixed in the stratosphere, we hypothesize that assuming a more realistic thermal structure between

the model top and TOA can improve accuracy of radiative flux calculations.

We explore the above hypothesis through single column experiments using RRTM in Section 2. Results from the single column experiments will then be applied to WRF during the test period described above and discussed in Section 3. A summary of the results and changes to WRF-RRTM scheme will be given in Section 4.

2. Single column experiments

a. Experimental setup

We use a stand-alone version of RRTM version 3.1 (available online at `http://rtweb.aer.com`). Control runs use the exact 36 vertical levels from AHW 2009, plus an additional level at the TOA that uses the same assumptions as WRF-RRTM. In other runs, we replace the additional TOA level by a buffer zone, with a variable number of levels, above the pressure at the model top (p_{top}). Experiments are performed using pressure increments of $\Delta p = -8, -4$, and -2 hPa in the buffer zone, inclusive of 1 hPa and 0 hPa. For example, $p_{top} = 20$ hPa with a pressure increment of $\Delta p = -4$ hPa includes buffer levels of 16, 12, 8, 4, 1, and 0 hPa. These pressure intervals are chosen as a compromise to resolving a realistic temperature profile while not significantly degrading computational efficiency.

Experiments are designed to account for various atmospheric conditions based on the standard MLW, MLS, SAW, and TROP atmospheres. In the buffer zone, temperature is extrapolated to the buffer levels using the vertically varying mean lapse rate from the standard MLW, MLS, SAW, and TROP profiles (recall Fig. 2a). Below the buffer zone, these initial temperature profiles are linearly interpolated to the given WRF vertical pressure levels

in the control and experiments. In the control case, volume mixing ratios of CO_2 and O_3 are converted from the average mass mixing ratios in the 2009 AHW experimental domain, while water vapor is converted from mean relative humidity; all other gaseous mixing ratios are set to zero as in WRF-RRTM. In the experiments, all gaseous mixing ratios are interpolated from their respective standard profiles. All cases assume clear-sky conditions.

b. Single column results

Fig. 3 shows the differences between the control and experimental $\dot{\theta}_{LW}$ at the top model level from their respective standard values. To explore a more complete range of solutions, experiments were repeated using $p_{top} = 0.2$, 0.5, 1, 5, 10, 20, 50, 100, 200, and 300 hPa using the same WRF η levels in all experiments. In the SAW control, the longwave cooling bias increases with increasing (decreasing) model top height (pressure), with a bias of -2 K day^{-1} for $p_{top} = 20$ hPa to values exceeding -20 K day^{-1} with $p_{top} = 1$ hPa (Fig. 3a). This result is rather surprising, and indicates the closer p_{top} and TOA, the stronger the bias. The buffer zone reduces the bias to $\pm$ 1 K day^{-1} for $1 < p_{top} < 200$, with the strongest reductions using $\Delta p = -4$ hPa. Similar patterns exist for the MLW, MLS, and TROP cases, where single column RRTM experiments show a substantial reduction in the $\dot{\theta}_{LW}$ bias (Fig. 3b-d).

The buffer itself may be problematic for model tops near the stratopause ($p_{top} < 5$ hPa). Note that although the bias remains large for such p_{top}, it is substantially reduced with a buffer. In the configuration here, as p_{top} decreases, there are fewer levels in a given layer near the stratopause than with a buffer for greater p_{top}. To test whether there is a sensitivity to the number of model levels near the stratopause, we repeat the above for the MLS experiment

(recall Fig. 3c), where biases for $p_{top} < 5$ hPa were largest. In the experiment here, we define WRF η levels to be of constant geopotential thickness (1.4 km) for $p < 20$ hPa based on the thickness of the AHW configuration near its model top of 20 hPa. The vertical level distribution from the above experiment is compared to the new distribution in Fig. 4a, and shows the relatively sparse distribution of vertical levels around the stratopause previously. Biases are reduced considerably for $p_{top} < 5$ hPa by having better vertical resolution near the stratopause (Fig. 4b). From further experiments (not shown), we can attribute the remaining disagreement to differences in the vertical resolution of the troposphere between the standard profile and experiments.

In addition to temperature, longwave radiative fluxes are also sensitive to concentrations of gaseous absorbers. Currently the effects of three gaseous absorbers are computed in WRF-RRTM: H_2O, CO_2, and O_3. Sensitivity tests (not shown) indicated that cooling rates respond largely to the change in CO_2 for $p_{top} < 200$ hPa; for $p_{top} > 200$ hPa, the largest response shifts to H_2O. There is a small response to changing O_3, except when p_{top} is near the stratopause. Thus, in addition to those for temperature, careful assumptions in CO_2 and H_2O in the buffer zone are important in obtaining accurate $\dot{\theta}_{LW}$ from RRTM. We next apply the buffer method to fully three-dimensional case using the AHW model.

3. Application to the WRF model

The new modifications to WRF-RRTM discussed in Section 2 are now applied to the same AHW forecasts discussed in Section 1. The model domain, configuration, and physics schemes are as in Torn (2010), where longwave radiation is computed with the RRTM

(Mlawer et al. 1997) and shortwave radiation with the National Aeronautics and Space Administration (NASA) Goddard shortwave radiation schemes (Chou and Suarez 1994). We composite a total of thirteen 6-hour forecasts, initialized every 12 h using Global Forecasting System (GFS) analyses beginning 16 August 2009 at 00 UTC and ending 22 August 2009 at 00 UTC with boundary conditions derived from GFS forecasts every 3 h. The simulations are performed on a Lambert Conformal projection, on a variably located fine-scale domain within the coarse domain (Fig. 1a) centered on the storms of interest for AHW 2009, using 424×325 x and y grid points respectively, and 12 km horizontal resolution.

Soon after the experiments began, an erroneous feature was found with regard to water vapor. It was found to arise in the handling of water vapor in the WRF Pre-Processing System (WPS) Version 3.0.1 when water vapor is not provided from the input data, such as the case with GFS grib data until January 2010, where water vapor extended only to 100 hPa. At levels where $p < 100$hPa, relative humidity was assumed to decrease proportionally with pressure, with a value of 5% at 50 hPa. This resulted in volume mixing ratios increasing with height to $\sim 2 \times 10^2$ ppmv at p_{top} for $p_{top} = 20$ hPa. Recall from Fig. 2c that volume mixing ratios should exhibit little variance $\sim$5 ppmv. We hereafter separate results into those where H_2O is left unchanged ('Without H2O adj.') and where H_2O is fixed to 5 ppmv at all levels where $p < 100$ hPa ('Full modifications').

At p_{top}, TROP and MLS $\dot{\theta}_{LW}$ is 63.0% and 66.7% lower than the control case, respectively (Fig. 5a). Adding the buffer zone reduces the cooling rates 48.7%, or $\sim$7 K day^{-1} with respect to the control at the top model level, with reductions to levels as far as $\sim$250 hPa (Fig. 5b). The water vapor adjustment reduces cooling rates an additional 2.5 K day^{-1} to cooling rates within $\pm$0.5 K day^{-1} of the standard cooling rates. Stronger cooling, up to 0.5 K day^{-1}, is

seen in the upper troposphere (∼200 hPa) when including the water vapor adjustment. A decrease in the downward flux from less stratospheric water vapor results in the enhanced cooling rates, and could lead to an increase in upper tropospheric clouds in areas close to saturation. Thus, the net changes eliminate the stratospheric cooling bias, and additionally correcting stratospheric water vapor reduces the upper-tropospheric warming trend (recall Fig. 1b,c). The spatial distribution of $\dot{\theta}_{LW}$ at the top model level exhibits a zonal cooling pattern in the control, with increased cooling rates ranging from $8-13$ K day^{-1} from south to north (Fig. 6a). This latitudinal $\dot{\theta}_{LW}$ pattern is associated with warmer stratospheric temperatures present during the summer over higher latitudes. The modifications in $\dot{\theta}_{LW}$ are reflected in $\frac{\partial\theta}{\partial t}$, with θ 2-4 K warmer on average at forecast hour six (Fig. 6b).

4. Summary

WRF (AHW) Forecasts initialized with both GFS and EnKF analyses exhibit a negative potential temperature tendency bias of up to 10 K day^{-1}, greatest at the model top. The bias was found to arise when using WRF with the RRTM longwave radiation physics scheme. With the expectation that gaseous longwave absorbers are well-mixed at levels where the bias is observed, it was hypothesized that previous assumptions of an isothermal layer between the model top and top of atmosphere lead to the flux divergence errors at the upper model boundary resulting in the bias.

Results reveal that the temperature bias can be reduced by (1) creating buffer levels between the model top and top of atmosphere using an extrapolated temperature profile based on the mean standard atmospheric lapse rate and (2) if necessary, setting water vapor mixing ratios for $p < 100$ hPa to a constant 5 ppmv. The former yields larger downward

radiative fluxes at the upper model boundary resulting in a smaller flux divergence, primarily affecting model levels close to the model top. The latter results in less cooling from reduced longwave absorption by water vapor molecules for $p < 100$ hPa, and further results in greater upper tropospheric cooling. The combined effects reduce longwave radiative cooling rates for $p_{top} > 5$ hPa to within ± 0.5 K day^{-1} of the standard rates obtained in the line-by-line clear-sky calculations of Clough and Iacono (1995). Cooling rates are now in more consistent agreement with those found using relatively high vertical resolution and upper boundaries of $\sim$0.1 hPa (Mlawer et al. 1997).

These results emphasize the importance of carefully specifying radiative fluxes at the upper boundaries of mesoscale models, especially those with model tops significantly below the top of atmosphere. They further emphasize the sensitivity of longwave heating to stratospheric trace gases, especially water vapor; great care should be placed on the assumptions of these concentrations when data is either unavailable or unreliable. Although the method here substantially reduces the magnitude of longwave biases for all model top levels tested, a considerable bias remains for model tops near the stratopause, which can be further reduced by increasing vertical resolution of the model and buffer levels near the stratopause.

Acknowledgments.

Support for the second author was by the Department of Energy through DOE-ARM grant DE-FG02-08ER64575.

REFERENCES

Chou, M. .-D. and M. J. Suarez, 1994: An efficient thermal infrared radiation parameterization for use in general circulation models. NASA Tech. Memo. 104606, 3. 85 pp.

Clough, S. A. and M. J. Iacono, 1995: Line-by-line calculation of atmopsheric fluxes and cooling rates .2. Application to carbon dioxide, ozone, methane, nitrous oxide, and the halocarbons. *J. Geophys. Res.*, **16 (D8)**, 16 519–16 535.

Collins, W. D., et al., 2006: The formulation and atmospheric simulation of the Community Atmosphere Model: CAM3. *J. Climate*, **19 (11)**, 2144–2161.

Davis, C. A., et al., 2008: Prediction of landfalling hurricanes with the Advanced Hurricane WRF Model. *Mon. Wea. Rev.*, **136 (6)**, 1990–2005.

Ellingson, R. G., J. Ellis, and S. Fels, 1991: The intercomparison of radiation codes used in climate models: Long-wave results. *JGR*, **96 (D5)**, 8929–8953.

Iacono, M. J., E. J. Mlawer, and S. A. Clough, 2000: Impact of an improved longwave radiation model, RRTM, on the energy budget and thermodynamic properties of the NCAR Community Climate Model, CCM3. *J. Geophys. Res.*, **105 (D11)**, 14,873–14,890.

Manabe, S. and R. F. Strickler, 1964: Thermal equilibrium of the atmosphere with a convective adjustment. *J. Atmos. Sci.*, **21**, 361–385.

Mass, C. F., D. Ovens, K. Westrick, and B. A. Colle, 2002: Does increasing horizontal resolution produce more skilled forecasts? the results of two years of real-time numerical weather prediction over the Pacific northwest. *Bull. Amer. Meteor. Soc.*, **83 (3)**, 407–+.

Mlawer, E. J., S. J. Taubman, P. D. Brown, M. J. Iacono, and S. A. Clough, 1997: Radiative transfer for inhomogeneous atmosphere: RRTM, a validated correlated-k model for the longwave. *J. Geophys. Res.*, **102 (D14)**, 16 663–16 682.

Skamarock, W. C., et al., 2008: A description of the advanced research WRF version 3. Tech. rep., NCAR.

Torn, R. D., 2010: Performance of a mesoscale ensemble Kalman filter during the NOAA high-resolution hurricane test. *Mon. Wea. Rev.*, Submitted.

Weisman, M. L., C. Davis, W. Wang, K. W. Manning, and J. B. Klemp, 2008: Experiences with 0-36 h explicit convective forecasts with the WRF-ARW model. **23 (3)**, 407–437.

List of Figures

3 Top of the model minus standard atmospheric longwave radiative heating rates as a function of model top pressure based upon standard (a) subarctic winter (SAW), (b) midlatitude winter (MLW), (c) midlatitude summer (MLS), and (d) tropical (TROP) atmospheric vertical profiles. The difference in the control experiment is shown in blue. Experiments using a pressure interval of −8 hPa, −4 hPa, and −2 hPa between the model top and top of the atmosphere (TOA) are shown with the dashed, solid, and dashed-dot red contours respectively. Note the contours shown are not continuous profiles. 17

4 (a) Distribution of WRF η levels as a function of pressure for the experiment using a pressure interval of −4 hPa (red) and when defining WRF η levels using a constant thickness of ∼1.4 km between 20 hPa and the model top (green) for a model top of 0.2 hPa. (b) Top of the model minus standard longwave radiative heating rates as a function of model top pressure using the vertical level levels shown in (a) based on the MLS atmospheric vertical profile. Note the contours shown in (b) are not continuous profiles. 18

5 Composite vertical potential temperature (a) heating rates and (b) differences from the control case of 6-hour forecasts initialized with GFS from 15 August 2009 at 00 UTC - 22 August 2009 at 00 UTC. The control case (no change in the RRTM longwave radiation scheme) is shown in black, while the standard tropical (TROP) and midlatitude summer (MLS) atmospheric profiles are shown by the blue and blue-dashed contours respectively. All profiles are averaged over the entire test domain (See Fig. 1a). 19

6 Composite potential temperature (a) heating rate differences and (b) changes in 6-hour forecasts at the top model level between the control and using the new longwave radiation (new buffer − control). In (b), values below 2 K are shaded in white. 20

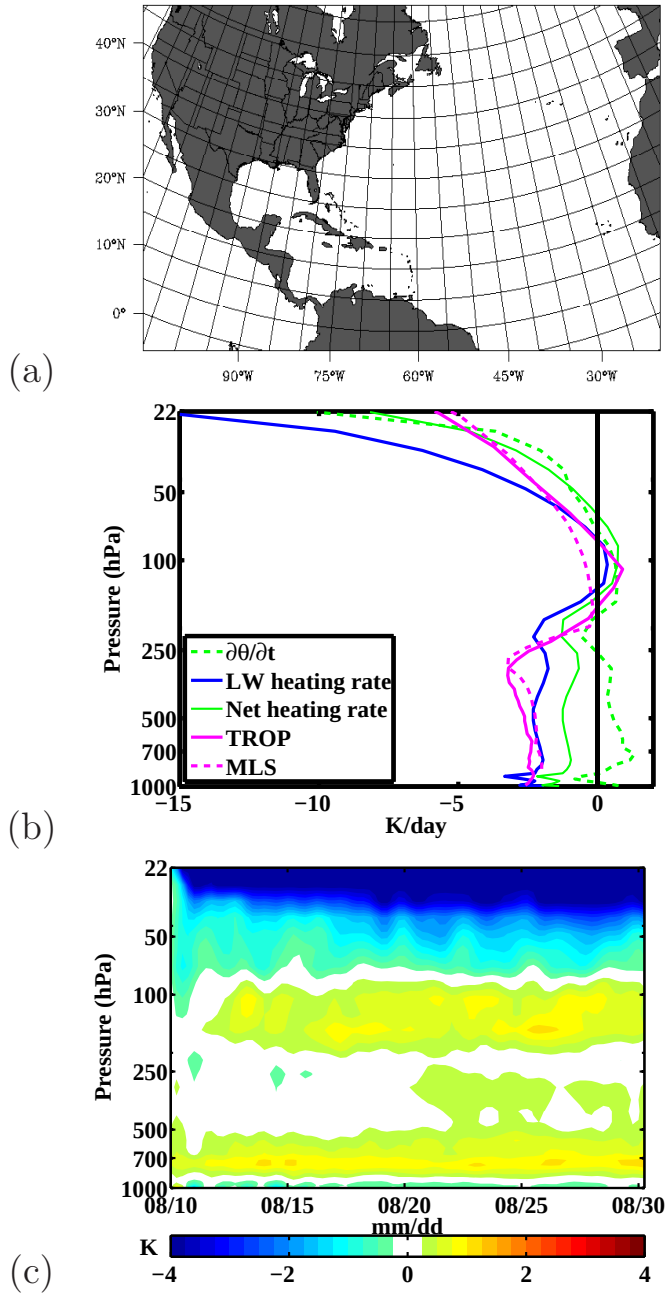

FIG. 1. (a) Numerical test domain, (b) composite potential temperature local time tendency, $\frac{\partial \theta}{\partial t}$ (green), longwave radiative potential temperature heating rate, $\dot{\theta}_{LW}$(blue), and net radiative potential temperature heating rate (green-dashed) compared with standard tropical (magenta) and midlatitude summer (magenta-dashed) longwave radiative potential temperature heating rate profiles from 6-hour forecasts initialized with GFS 16 August 2009 at 00 UTC - 22 August at 00 UTC. Profiles are averaged over the entire test domain. Time-height section from the same domain, but from a data assimilation cycling period from 10 August 2009 at 00 UTC - 30 August 06 UTC using an Ensemble Kalman Filter (EnKF) with (c) potential temperature bias with respect to GFS (EnKF − GFS).

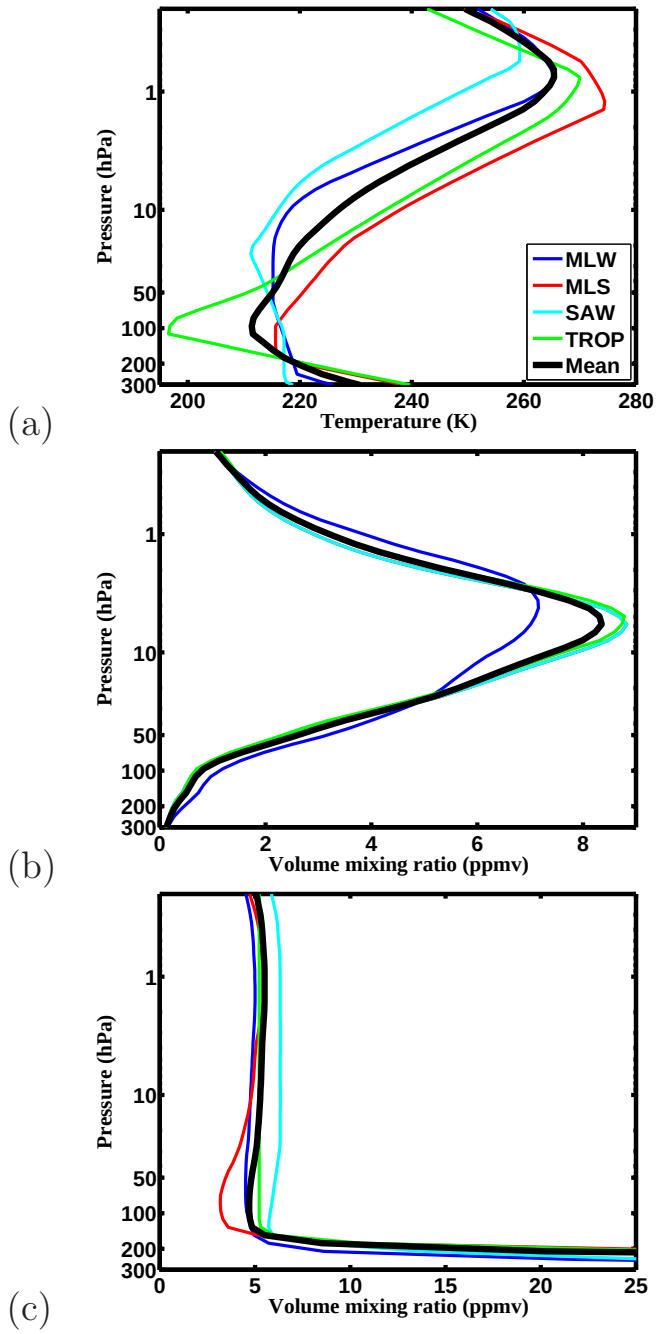

FIG. 2. Standard midlatitude winter (MLW, blue), midlatitude summer (MLS, red), subarctic winter (SAW, cyan), tropical (TROP, green), and mean (bold black) vertical profiles of (a) temperature (K), (b) ozone (ppmv), and (c) water vapor (ppmv).

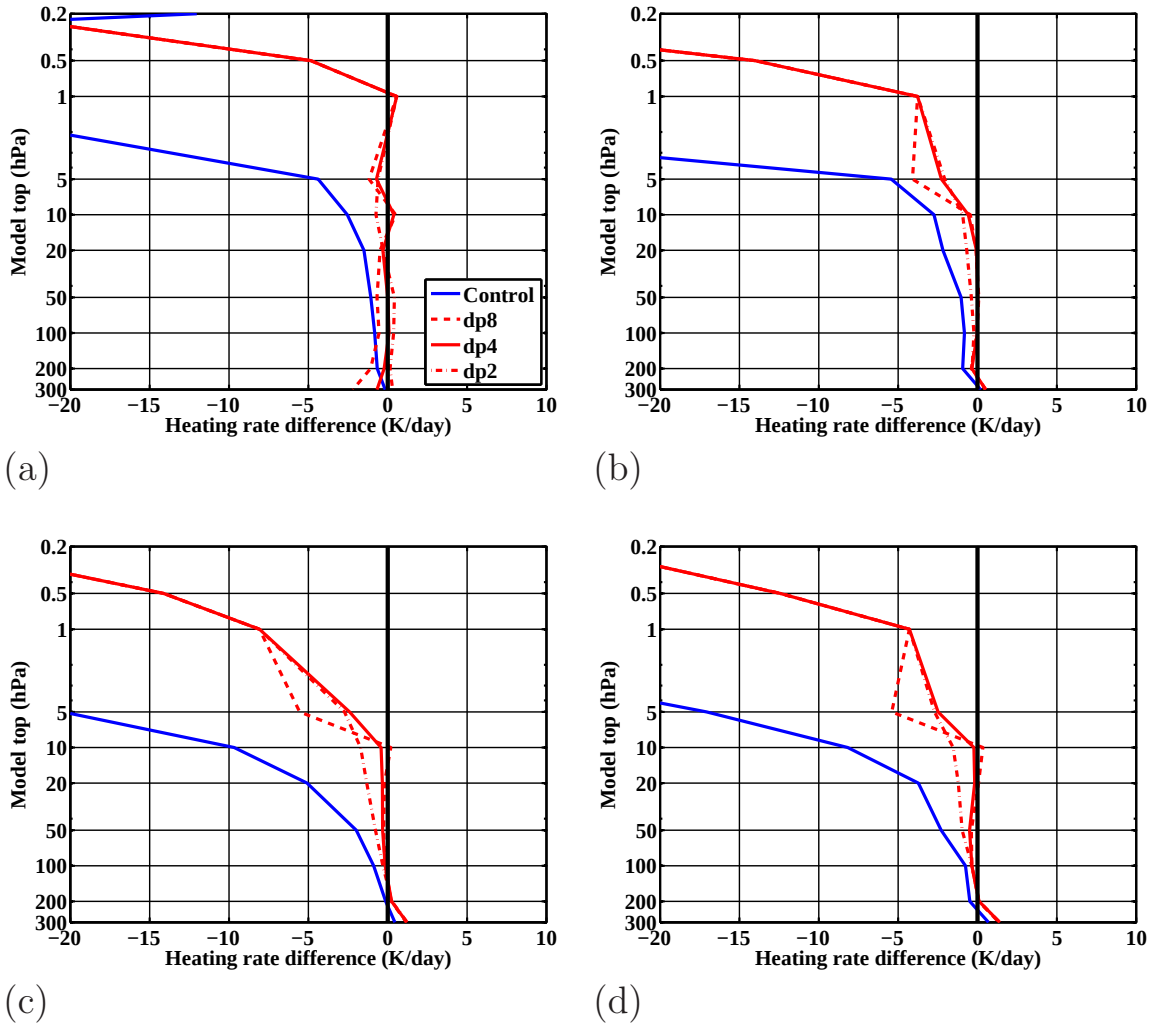

FIG. 3. Top of the model minus standard atmospheric longwave radiative heating rates as a function of model top pressure based upon standard (a) subarctic winter (SAW), (b) midlatitude winter (MLW), (c) midlatitude summer (MLS), and (d) tropical (TROP) atmospheric vertical profiles. The difference in the control experiment is shown in blue. Experiments using a pressure interval of −8 hPa, −4 hPa, and −2 hPa between the model top and top of the atmosphere (TOA) are shown with the dashed, solid, and dashed-dot red contours respectively. Note the contours shown are not continuous profiles.

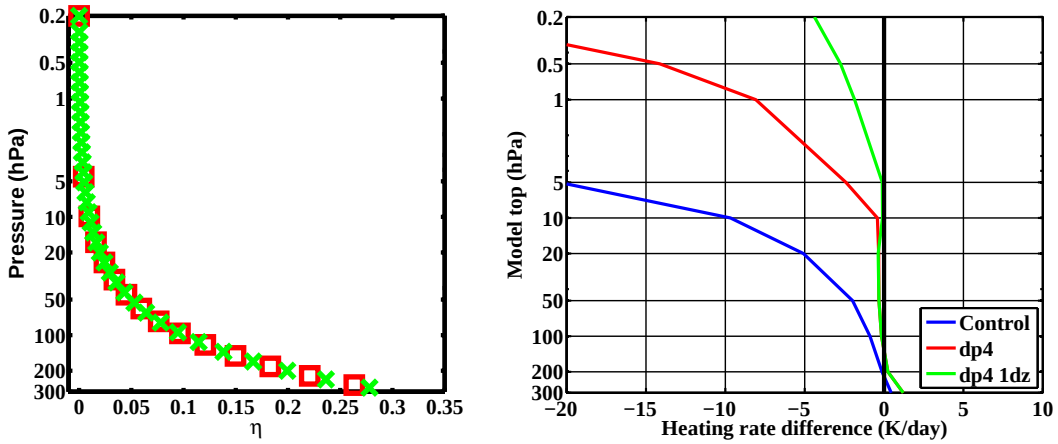

FIG. 4. (a) Distribution of WRF η levels as a function of pressure for the experiment using a pressure interval of -4 hPa (red) and when defining WRF η levels using a constant thickness of $\sim$1.4 km between 20 hPa and the model top (green) for a model top of 0.2 hPa. (b) Top of the model minus standard longwave radiative heating rates as a function of model top pressure using the vertical level levels shown in (a) based on the MLS atmospheric vertical profile. Note the contours shown in (b) are not continuous profiles.

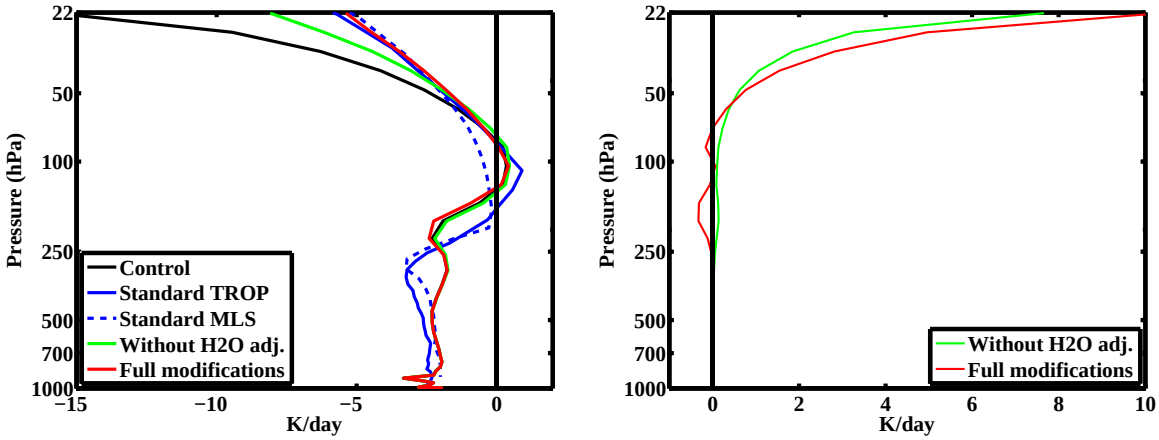

FIG. 5. Composite vertical potential temperature (a) heating rates and (b) differences from the control case of 6-hour forecasts initialized with GFS from 15 August 2009 at 00 UTC - 22 August 2009 at 00 UTC. The control case (no change in the RRTM longwave radiation scheme) is shown in black, while the standard tropical (TROP) and midlatitude summer (MLS) atmospheric profiles are shown by the blue and blue-dashed contours respectively. All profiles are averaged over the entire test domain (See Fig. 1a).

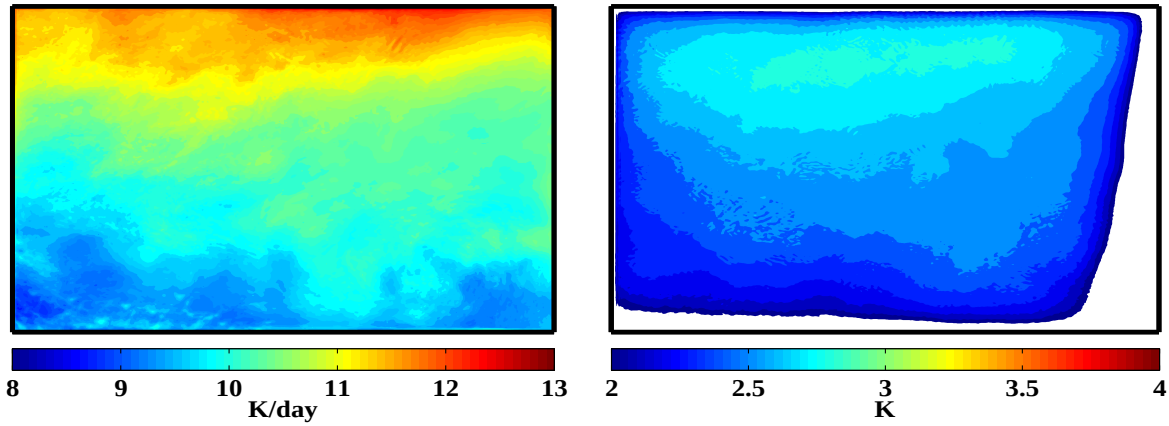

(a) (b)

FIG. 6. Composite potential temperature (a) heating rate differences and (b) changes in 6-hour forecasts at the top model level between the control and using the new longwave radiation (new buffer − control). In (b), values below 2 K are shaded in white.